Analytical and Bioanalytical Chemistry
https://doi.org/10.1007/s00216-021-03174-1

RESEARCH PAPER

# Mass shift in mass spectrometry imaging: comprehensive analysis and practical corrective workflow

Andréa McCann[1] · Sophie Rappe[1] · Raphaël La Rocca[1] · Mathieu Tiquet[1] · Loïc Quinton[1] · Gauthier Eppe[1] · Johann Far[1] · Edwin De Pauw[1] · Christopher Kune[1]

Received: 14 October 2020 / Revised: 22 December 2020 / Accepted: 13 January 2021


## Abstract

MALDI mass spectrometry imaging (MSI) allows the mapping and the tentative identification of compounds based on their *m/z* value. In typical MSI, a spectrum is taken at incremental 2D coordinates (pixels) across a sample surface. Single pixel mass spectra show the resolving power of the mass analyzer. Mass shift, i.e., variations of the *m/z* of the same ion(s), may occur from one pixel to another. The superposition of shifted masses from individual pixels peaks apparently degrades the resolution and the mass accuracy in the average spectrum. This leads to low confidence annotations and biased localization in the image. Besides the intrinsic performances of the analyzer, the sample properties (local composition, thickness, matrix deposition) and the calibration method are sources of mass shift. Here, we report a critical analysis and recommendations to mitigate these sources of mass shift. Mass shift 2D distributions were mapped to illustrate its effect and explore systematically its origin. Adapting the sample preparation, carefully selecting the data acquisition settings, and wisely applying post-processing methods (i.e., *m/z* realignment or individual *m/z* recalibration pixel by pixel) are key factors to lower the mass shift and to improve image quality and annotations. A recommended workflow, resulting from a comprehensive analysis, was successfully applied to several complex samples acquired on both MALDI ToF and MALDI FT-ICR instruments.

**Keywords** Mass spectrometry imaging · FT-ICR · Mass shift · Data recalibration · Time of flight · Mass accuracy

## Introduction

Mass spectrometry imaging (MSI) is a powerful mass spectrometry (MS) method to visualize 2D molecular species distribution in a sample. A mass spectrometry image consists of a set of mass spectra obtained from a thin section of the sample moved step-by-step in a regular grid under an ionization source. Each spot, also called pixel, contains a whole mass spectrum. A common method to produce ions at different spots is the use of laser-based ion source, such as laser desorption ionization (LDI), surface-assisted laser desorption ionization (SALDI), and especially matrix-assisted laser desorption ionization (MALDI). Desorption electrospray ionization (DESI) and secondary ion mass spectrometry are also popular ion sources fitting well with mass spectrometry imaging [1]. Less frequently, images are obtained in microscopic mode using a position sensitive detector [2]. In scanning MSI methods, all the individual mass spectra (i.e., from all pixels) are compiled to produce 2D maps that can be reconstructed for each *m/z* [3] or for families of compounds [4].

The use of maximum mass accuracy and sufficient mass resolving power allows a molecular formula to be assigned to each peak, as long as the peak is free of isobaric interferences and detected with a sufficient sensitivity [5], while MS/MS strategies are usually required to resolve atomic connectivity and to identify the ions with more confidence [6–8]. Any additional descriptors, such as the collision cross section (i.e., from ion mobility MS) can help in confirming the identification without requiring MS/MS steps [9–11].

Peak annotation in mass spectrometry imaging will therefore rely primarily on the *m/z* values and isotopic ratios. MSI gains its full power when accurate mass determination at high

Published in the topical collection *Mass Spectrometry Imaging 2.0* with guest editors Shane R. Ellis and Tiffany Porta Siegel.

Andréa McCann and Sophie Rappe are co-first authors of this paper.

Andréa McCann and Sophie Rappe contributed equally to this work.

✉ Christopher Kune
c.kune@uliege.be

[1] Mass Spectrometry Laboratory, MolSys Research Unit, Department of Chemistry, University of Liège, Allée du Six Août, 11 – Quartier Agora, 4000 Liège, Belgium

Published online: 30 January 2021

resolving power can be obtained on the whole image. This allows the optimum use of a common step in MSI; the construction of an average spectrum from the individual pixel spectra. The average spectrum facilitates the obtention of a quick global view of *m/z* distributions and the evaluation of the data quality. Peak annotation can then be performed from the average spectrum and reliable *m/z* images can be reconstructed. The individual spectrum quality of a pixel corresponds to the performances of the MS analyzer, such as time of flight (ToF), Fourier transform ion cyclotron resonance (FT-ICR), and Orbitrap mass spectrometers. However, the exact mass may be shifted from one pixel to another leading to peak broadening in the average spectrum. Both instrument and sample characteristics can affect the mass accuracy from one pixel to another. Mass analyzers are subjected to physical limitations linked to their ion optics, which need to be properly considered for successful mass spectrometry imaging experiment [12–19]. In ToF instruments, a variation in sample height may affect the ion trajectory and consequently the mass accuracy. In FT-ICR instruments, a high ion density may cause space charge effects in the ICR cell, resulting in mass shifts. In the presence of mass shift, higher tolerance levels in terms of mass accuracy are required to reconstruct the relevant image of a targeted ion, increasing the risk of isobaric interference and miss-annotated peaks.

Here, we present a systematic study aimed at understanding, visualizing, reducing, and correcting mass shift to alleviate an important limitation in MSI. The results are presented to provide users general recommendations to improve mass accuracy of the MSI data by preventing or, at least, by reducing the experimental mass shift between pixels. To achieve this purpose, we have pinpointed the main key factors causing mass shift according to the type of MALDI MS instruments: sample thickness for the MALDI ToF (linear geometry) and sample heterogeneity for MALDI FT-ICR fitted with the dynamically harmonized ICR cell. Nonetheless, other MALDI MS instruments used for MALDI mass spectrometry imaging will also benefit from these recommendations. Our recommendations cover sample preparation to the optimization of MS parameters for data acquisition. We also propose data post-processing methods to perform the *m/z* realignment and *m/z* recalibration of the spectra pixel by pixel. Finally, we have applied our recommendations for various complex and problematic samples where we have favorably improved the mass accuracy in the MSI average spectrum leading to improved peak annotations.

## Materials and methods

### Material

MALDI matrix α-cyano-4-hydroxycinnamic acid (HCCA) MALDI matrix 2,5-Dihydroxybenzoic acid (DHB), trifluoroacteic acid (TFA), formic acid, ethyl acetate, chloroform, and absolute ethanol were purchased from Sigma-Aldrich (Overijse, Belgium). Acetonitrile and methanol were LC-MS grade from Biosolve (Valkenswaard, Netherlands). Poly(ethylene oxide) monomethylether ($CH_3O$-$(CH_2O)_n$-OH) having an average nominal mass of 750 g/mol and sodium chloride were purchased from Sigma-Aldrich (Overijse, Belgium). Select Agar™ under powder form was obtained from Invitrogen (Thermo Fisher Scientific, Waltham, MA, USA). Standards Ceramide Sphingoid mix II (25 μM) were purchased from Avanti polar lipid (from local exclusive redistributor Sigma-Aldrich). Indium tin oxide (ITO)-coated glass slides were purchased from Bruker Daltonics (Bremen, Germany). n-Hexane was purchased from LGC (Queens Roads, Teddington, Middlesex, UK).

### Sample preparation for MALDI MSI

**PEO synthetic samples** PEO stock solution was prepared by dissolving PEO in ACN 10 μM NaCl to reach a concentration of 100 μM. A synthetic sample imitating heterogeneous sample in terms of molecular composition using different concentrations of PEO was built. The PEO solution was diluted twice 10 times in series in ACN to obtain three PEO solutions of 100 μM, 10 μM, and 1 μM (assuming non-dispersed distribution of PEO having a molecular weight of 750 g/mol). Each PEO solution was then sprayed onto different regions of an ITO glass slide with the SunCollect instrument (SunChrom, Friedrichsdorf, Germany). For each region, 10 layers of PEO were sprayed at a linear gradient of flow rate from 10 to 60 μL/min. A purposely designed synthetic sample for the study of topology variation effect was prepared using 1.5% agar powder diluted in $H_20$ spiked with 5 mM NaCl and PEO stock solution to reach a final PEO concentration of 10 μM. The liquid agar solution was then poured in 10-cm plastic petri dishes with various volumes of liquid agar (10 mL, 15 mL, 20 mL, 25 mL, depicted as T1, T2, T3, and T4 respectively) to obtain different agar thicknesses. The agar was then left to cool until solidified. Small rectangles of agar were cut and fixed onto $75 \times 25$-$mm^2$ ITO-coated conductive glass slides previously covered with double-sided copper tape (StructureProbe INC, West Chester, PA, USA). The ITO slides were placed under vacuum at 70 mbar until the agar dried.

**Cryosectioning** Mouse brain tissue (kindly provided by the Department of Psychiatry and Neuropsychology, School for Mental Health and Neuroscience from Maastricht University) and salmon brain (from a local retailer) homogenate slices destined to mass spectrometry imaging were prepared using a cryomicrotome (Cryostar NX70, Thermo Fischer Scientific, Waltham, MA, USA) with temperatures set at − 20 °C for the sample holder and − 10 °C for the SEC 35e razor blade. Mouse brain tissue slices were cut at a thickness of 10 μm while salmon brain homogenates were cut at 16 μm.

Additionally, some salmon brain homogenate slices were cut after inducing bevel-like slices in the sample holder horizontal axis where the thickest part was estimated to be 50 ± 10 μm. All slices were thawed-mounted on ITO glass slides. The samples were then dried in a vacuum desiccator for 15 min or until visible dryness.

**Bacterial strains, medium, and culture conditions** The strains used for this study were *Bacillus velezensis GA1* and *Pseudomonas sp. CMR12a*. Five micoliters of both bacterial cell suspension (OD 600 nm = 0.1) was spotted at 10-mm distance on a semisolid agar-based root exudates mimicking medium [20] and incubated for 48 h at 25 °C. Microbial colonies on agar and region of interest were cut from the Petri dish and transferred to the target ITO plate, previously covered with double-sided conductive copper tape. This assembly was then placed in a vacuum desiccator at 70 mbar until dryness overnight [21].

**Matrix deposition** HCCA matrix was sprayed on PEO samples, bacteria sample, and brain samples (mouse brain tissue and salmon brain homogenates). HCCA matrix was mixed in 70:30 ACN:water v:v with 0.2% TFA to reach a final concentration of 5 mg/mL. In total, 10 layers of HCCA matrix were sprayed onto the ITO slides with the SunCollect instrument (SunChrom, Friedrichsdorf, Germany). The first layer was sprayed at a flow rate of 10 μL/min. Flow rate was increased by 10 μL/min after each layer until reaching 60 μL/min.

**Standard lipid samples with different crystallization methods** The heterogeneous crystallization sample was obtained by diluting the standard Ceramide Sphingoid mix II (25 μM) tenfold in an ethanol-chloroform mixture (50:50 v:v). The DHB matrix was diluted at 100 mg/mL in an ethyl acetate-hexane-formic acid mixture (98.9:1:0.1 v:v:v). One microliter of diluted lipids standard (Ceramide Sphingoid mix II) was spotted onto an ITO slide. One microliter of matrix solution was then spotted onto the sample and mixed thoroughly with the dried droplet crystallization method. Samples were air-dried at room temperature. The sizes of crystals were determined using an inverted optical microscope Olympus IX 81 (Olympus, Aartselaar, Belgium). Sample topology was investigated by scanning electron microscopy using the XL30 FEG-ESEM instrument (Field Electron and Ion Company, Hillsboro, OR, USA). Two homogeneous crystallization samples were prepared alongside by spotting 1 μL of diluted lipids standard on each ITO slide. A 10 mg/mL solution of matrix DHB diluted in an ethyl acetate-hexane-formic acid mixture (98.9:1:0.1 v:v:v) was then sprayed onto the first ITO slide with the HTX TM-Sprayer (HTX Technologies, LLC, Chapel Hill, NC, USA). In total, 25 layers of matrix solution were applied at a flow rate of 5 μL/min. Fifty milligrams of DHB matrix dissolved in 2 mL of methanol was also applied by sublimation using the HTX Sublimator (HTX technologies, Chapel Hill, NC, USA) to the second ITO slide. The solvent was evaporated during preheating of the chamber at 65 °C and the sublimation of DHB occurred at 160 °C under vacuum for 160 s.

## MALDI MSI methods

**Bacteria co-culture, synthetic PEO, and agar samples** Mass spectrometry images were produced in positive ionization mode from *m/z* 300 to 2000 using either FT-ICR instrument (solariX XR 9.4T, Bruker Daltonics, Bremen, Germany) fitted the dual ESI/MALDI ion sources and SmartBeam laser or ToF instrument (rapifleX, Bruker Daltonics, Bremen, Germany) fitted with the smartbeam™ 3D laser. Laser parameters (laser power, shots number, and repetition rate) were optimized on both instruments to ensure the correct detection of the minimum concentration of PEG (1 μM) at *S/N* above 3 according to the FlexImaging 5.0 software (Bruker). Both instruments were calibrated from *m/z* 300 to 2000 in the same conditions as the mass spectrometry images using red phosphorous freshly suspended in acetone and directly spotted onto each ITO glass slide. Pixel step size for the surface raster was set to 200 μm.

Bacteria imaging was performed with a raster of 100 μm using 20 laser shots set and repetition rate of 5 kHz for both the solariX XR and rapifleX instruments. Laser power was set at 40% on the rapifleX instrument and at 70% on the solariX XR instrument. Two other images were acquired with either 200 or 2000 laser shots to estimate the effect of mass shift dependence in regard to the amount of the injected ions per packet.

**Mouse brain tissue and salmon brain homogenate samples** The mouse brain tissue images were acquired on the solariX XR FT-ICR MS using a lateral laser resolution of 60 μm and laser parameters of 400 shots at 1000 Hz with a power of 70%. Salmon brain homogenate images were acquired on the rapifleX ToF MS and on the solariX XR FT-ICR MS instruments using a raster width of 100 μm. FT-ICR laser parameters were set as 20 shots at 200 Hz with a laser power of 70%. The rapifleX laser parameters were set to 500 laser shots at 5 kHz.

**Lipid standard sample and co-crystallization experiments** Data acquisitions of lipid samples were performed using the rapifleX in positive mode ionization at *m/z* 100 to 1200. Laser power was set to 60%. The MSI data were acquired with a spatial resolution of 25 μm for the dried droplet sample and 10 μm for sprayed matrix and matrix sublimation deposition, using 1000 laser shots per pixel at 10 kHz frequency.

## Data processing

Data were reprocessed using FlexImaging 5.0 (Bruker Daltonics, Bremen, Germany) and SCiLS (Bruker Daltonics,

Bremen, Germany). MSI data recalibration was carried out using our in-house algorithm [22] (see also Supplementary Information (ESM)). The image of the mass shift dispersion and computation of the maximum mass shift of the dataset were performed using in-house Python software (using Numpy, Scipy, Tkinter, and Matplotlib numerical packages) written by C. Kune [4] and modified to fit this purpose.

## Result and discussions

### Mass shift visualization

The difference between the experimental accurate *m/z* values of a target ion and its theoretical value (computed from its molecular formula) is called the mass accuracy. Variations of the mass accuracy may occur from one pixel to another due to the limitations of the instrument, which will be diagnosed in this study on experimental conditions. Those mass accuracy variations affect the average mass spectrum, extending the width of *m/z* distribution and thus apparently decreasing the mass resolving power below the instrument specifications. In addition, the apex of the peaks in the average spectrum may differ from those of the individual spectra, due to the use of a unique calibration covering the whole MSI data. Consequently, the peak apex in the average spectrum may deviate significantly from the expected *m/z*, resulting in poor accuracy compared to manufacturing specifications. The peak apex of the *m/z* distribution from the average mass spectrum is often used to estimate the global mass accuracy of a MSI data without considering mass shift effect. Both mass accuracy and mass shift in the average spectrum should be considered as two criteria for evaluating the quality of a MSI data. Since the average mass spectrum is very frequently used as the starting point for extracting reconstructed *m/z* images from MSI data, it is crucial to first understand the contribution of the experimental settings for the optimization of these two criteria before their correction involving data post-processing.

Two worst-case scenarios illustrating mass shift issues on MSI data analysis are reported in Fig. 1. The first example (Fig. 1a) concerns the signal monitoring of the $Na^+$ adduct of Lactosyl $C_{12}$ ceramide ([Lactosyl $C_{12}$ + Na]$^+$, *m/z* 828.5444), present in the Ceramide Sphingoid mix II standard lipid solution co-crystallized in DHB matrix. The mass spectrometry images were acquired using a rapifleX MALDI ToF instrument. The crystallization of the sample was deliberately intended to produce different crystal shapes. As expected, one observes the formation of matrix crystals exhibiting different sizes from a few micrometers to 200–300 μm wide and approximately 40 μm of height variations, determined with an optical inverted microscope. The mass accuracy in the average mass spectrum (around 100 ppm) and the final resolving power were very poor (2500 FWHM at *m/z* 828.5444)). This mass accuracy is far below the expected

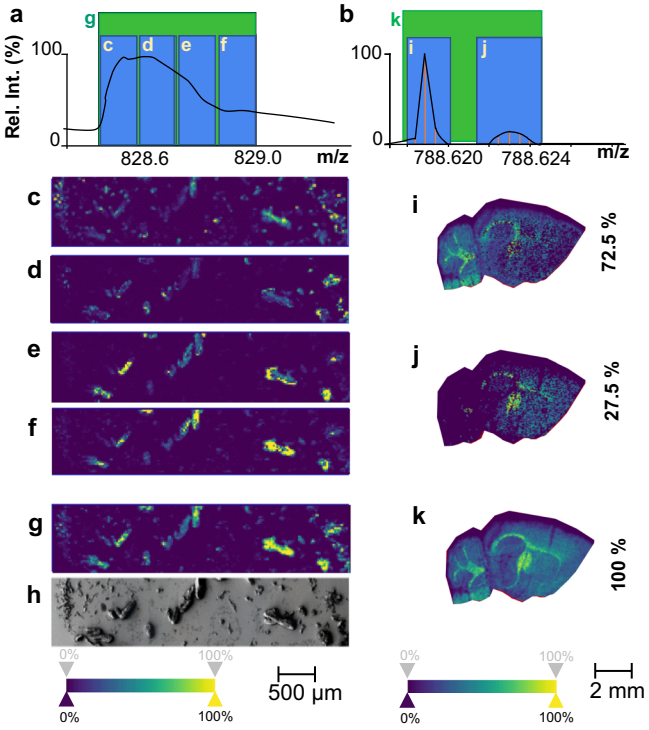


**Fig. 1** Ion images reconstructed from *m/z* selection in the average MS spectrum for MSI data subjected to mass shift. **a** Distribution of Lactosyl C12 ceramide with sodium adduct (*m/z* 828.5444) in a dried droplet of standard lipid solution with DHB matrix. An electron microscopy image is displayed for the dried droplet of standard lipid solution (h) to show the high heterogeneity of the sample crystallization. **b** Distribution of protonated PC 36:1 (*m/z* 788.6164) in mouse brain tissue. For both samples, the partial images reconstructed from *m/z* selections (c, d, e, f for sample a and i, j for sample b) and the global images (g and k) are reported showing the importance of the *m/z* tolerance for relevant MSI image reconstruction

manufacturer's specification of the rapifleX's ToF analyzer, which under optimal condition and in reflectron mode, should provide a mass accuracy less than or equal to 5 ppm and a resolving power greater than or equal to 13,000 FWHM for Bradykinin 2-9 at *m/z* 904. Different consecutive *m/z* ranges (0.1400 u) were taken from the broad peaks in the average spectrum and corresponding images were reconstructed. The combination of all the *m/z* areas within a single broad peak allows reconstructing of the full image. In this example, [Lactosyl $C_{12}$ + Na]$^+$ is detected within a relatively large range of *m/z* values (about 0.5 u) depending on the sample localization. The whole MS distribution of [Lactosyl $C_{12}$ + Na]$^+$ (Fig. 1g) must be taken into account to capture the entire map of this compound. It is interesting to note that the MS images reconstructed by sectioning different *m/z* values (Fig. 1c, d, e and f) highlight different crystals based on their size, suggesting a correlation between crystals size and mass shifts (this will be discussed in the section dedicated to sample thicknesses). Mass shifts could also be observed, in a lesser extent (0.005 u), using the solariX XR FT-ICR instrument, as reported in Fig. 1b (mouse brain tissue section MSI). The investigated ion in this study has been putatively identified as the protonated phosphatidylcholine PC 36:1

($m/z$ = 788.6164) after a bulk structure search on the LIPID MAPS Structure Database (LMSD) [23]. The effect of mass shift reported in this figure is even more pronounced than the previous one since two apparently distinct $m/z$ peaks were observed for a single ion. The reconstructed ion images from each MS peak (selections i and j in Fig. 1b) lead to partial but complementary images with a pixel recovery score of 72.5% and 27.5% respectively. Here again, the whole signal of protonated PC 36:1 should be taken into account to reconstruct the entire ion image of this tissue section (k in Fig. 1b).

These two examples show that the mass shift impairs the mass resolving power in the average spectrum, and results in a potentially compromised ion annotation. On the FT-ICR example, individual spectra comply with the expected resolution, but the mass measurement accuracy may differ. The degraded mass resolving power in the average mass spectrum suggests therefore that this occurs upon summation of the individual spectra. On the ToF example, some individual spectra showed broader peaks than expected by the instrument resolution, suggesting additional factors influencing the average MS spectrum resolution.

Before attempting any correction, mass shift visualization by mapping the variation of the experimental $m/z$ peaks for all the pixels is a fast and easy way to figure how severe could be this mass shift in your mass spectrometry imaging data.

Mass shift amplitude can be estimated from the variation of the measured $m/z$ value of the same ion in each pixel. For this purpose, the measured $m/z$ value in each pixel should be characterized as the $m/z$ peak apex or directly obtained from centroid MS spectra (i.e., bar charts obtained after peak-picking process). This visualization of the mass shift can be computed for any MS analyzer. Because mass shift estimation relies on centroid $m/z$ distribution only, the instrument resolving power does not affect the calculation. Mass shift value can be plotted in a 2D heatmap (i.e., mass shift value in function of the $XY$ position of the pixel) allowing the visualization of the mass shift in function of the localization in the sample. The mass shift heatmaps presented in this work have been generated with an in-house software. Briefly, this software performed a peak picking in all pixels of the MSI data. The mass shift is calculated according to Eq. 1 in a very similar fashion as the mass accuracy calculation between the centroid peak of the computed pixel and the average mass spectrum. The main difference with the conventional mass accuracy equation relies on the chosen mass reference value. This can be the theoretical $m/z$ value of a target ion or an arbitrary $m/z$ value of this peak, e.g., the smallest $m/z$ value reported for this peak, as long as the chosen mass reference is explicitly and initially defined by the users. The output of this script is a list of mass shifts (i.e., mass shift according to the pixel identifier) and a mass shift heatmap (i.e., mass shift plotted according to the XY position in the sample). This script also allows the extraction of the peak width (e.g., at 10% of its absolute intensity of full width at half maximum) to monitor the MS peak width evolution from pixel to pixel in addition to mass shifts.

$$\text{masserror}_{\text{rel.}}(\text{ppm}) = \frac{m/z_{\text{exp.}} - m/z_{\text{exact}}}{m/z_{\text{exact}}} \times 10^6 \quad (1)$$

## Mass shift understanding

### Sample composition variation

Unlike ToF, ICR instruments are ion trap mass analyzers. FT-ICR instruments infer the $m/z$ ratio of ions by measuring the angular frequency of the ions under high magnetic field due to the Lorentz force. The angular frequencies of the ions depend solely on the $m/z$ and the magnetic field strength. Ion detection is carried out by the mirror current of the spinning ions in proximity with the detection plates of the ICR cell after excitation by the excitation plates. However, the trapped ions inside the ICR cell may be subject to space charge effects, affecting the angular frequencies of the ions.

Space charge effects on the mass shift during MSI experiments by MALDI FT-ICR were studied using various concentrations of PEO sprayed onto an ITO glass slide and covered with HCCA matrix. Ion count and mass shift evolution of the most intense PEO ion $[PEO17+Na]^+$ ($m/z$ = 803.4616) were monitored according to the different zones of the sample slide with both MALDI ToF and MALDI FT-ICR, and are summarized in Table 1. The mass shift (in ppm) was calculated according to Eq. 1, using the peak apex in the average mass spectrum of 1 μM $[PEO17+Na]^+$ as $m/z$ reference.

As expected, Fig. S1 (see ESM) and Table 1 illustrate that the increase of PEO concentration leads to an increase of the total ion current (TIC), especially for the MALDI FT-ICR instruments (i.e., solariX XR instrument). MSI experiment performed with the solariX XR 9.4T (see Table 1 and ESM Fig. S1) shows that the $m/z$ values are shifted to higher values when the TIC increase. A linear correlation between the TIC and the shift of the measured mass was observed in perfect agreement with the report from E. Nikolaev and coworkers [14]. A significant mass shift of 2 ± 0.1 ppm (specification of the solariX XR is 0.5 ppm RMS) is observed between the $m/z$ signal in the zone with the highest PEO concentration (PEO concentration = 100 μM, TIC = $1.79\times10^8$ cps) and the reference zone (PEO concentration = 1 μM, TIC = $8.35\times10^7$ cps). Moderate mass shift is also observed at the intermediate concentration level (PEO concentration = 10 μM, mass shift = 0.5 ± 0.1 ppm, TIC = $9.98\times10^7$ cps). Contrary to the solariX XR experiment, no correlation between mass shift and TIC was observed in MALDI ToF MSI data. This confirms that the $m/z$ measurement is almost unaffected by the space charge effect in the ToF analyzer. This model confirms that the space charge effect is an inherent issue for high-resolution instrument trapping ions such

**Table 1** Effect of concentration of polyethylene oxide methyl ether on the generated total ion current (TIC) on the experimental mass shift. Mass reference was (PEO) $[PEO17+Na]^+$ ($m/z$ = 803.4616). MALDI ToF was a rapifleX and the MALDI FT-ICR was a solariX XR 9.4T. See related Fig. S1 in ESM

| Mass analyzers | | Polyethylene oxide methyl ether concentration | | | | | |
|---|---|---|---|---|---|---|---|
| | | TIC (cps) | | | Mass shift (ppm) | | |
| | | 1 μM | 10 μM | 100 μM | 1 μM | 10 μM | 100 μM |
| ToF | Average | 116 | 115 | 171 | 0.00 | 1.51 | 1.68 |
| | Standard deviation | ±3 | ±3 | ±4 | ±1.13 | ±0.64 | ±0.67 |
| FT-ICR | Average | $8.35\times10^7$ | $9.98\times10^7$ | $1.79\times10^8$ | 0.00 | 0.37 | 2.03 |
| | Standard deviation | $\pm5.45\times10^5$ | $\pm6.78\times10^5$ | $\pm1.10\times10^6$ | ±0.07 | ±0.05 | ±0.06 |

as FT-ICR devices. Nevertheless, the correlation between the mass shift and the TIC is instrument-dependent and must be determined for each type of device (e.g., TIC effect on mass shift could be different on various FT-ICR instruments especially when using a different supra-conducting magnet).

## Sample thickness

ToF mass analyzers are scanning instruments, meaning that the ions are transmitted through the mass analyzer to determine their $m/z$ ratios. In these instruments, the mass is calculated from the ion velocity (specifically, the time to travel a given distance) when they are accelerated to a common kinetic energy in a vacuum. Any deviation from this acceleration will modify the measured $m/z$ value. Delayed extraction associated with the use of a reflectron makes ToF instruments fast and efficient mass analyzers. However, the kinetic energy provided by the ions is critically affected by the position in the source of the surface of the sample to be ionized [24]. Variations in the sample's surface topology will produce packets of ions with different kinetic energies. To analyze the contribution of the surface topology to the mass shift, we used polyethylene oxide methyl ether (PEO) polymer embedded in various thicknesses of agar medium that we dried and recovered with HCCA matrix before mass spectrometry imaging.

Rough surface samples are commonly known to cause a loss in mass accuracy [16, 17, 25] and a drop in ionization efficiency [26, 27]. Mass shifts for the $[PEO17+Na]^+$ ($m/z$ = 803.4616) were calculated (in ppm) from Eq. 1 (using the average $m/z$ value of $[PEO17+Na]^+$ in the thinnest zone of the sample, depicted as "T1" as the reference value). The calculated mass shifts are then presented in Table 2 (see ESM Fig. S1), for both MALDI ToF and MALDI FT-ICR instruments. In a ToF instrument, the topology effect is particularly visible, with a relative mass shift reaching up to − 350 ppm. The observed trends showed that the higher the sample surface, the smaller the measured $m/z$ value, as already mentioned elsewhere [24].

In the MALDI FT-ICR instrument, a relatively limited mass shift is observed (± 0.5 ppm, i.e., under the instrument specification), independently of the sample surface. In this experiment, the small range of intensity variation (i.e., from $6.81\times10^7$ to $7.42\times10^7$ cps) seems to be low enough to avoid mass shift due to significant space charge effect (note that these values are only applicable for the FT-ICR instrument used, i.e., Bruker's solariX XR). From these results, one can assume that sample topology has a negligible impact on the mass shift when using FT-ICR instruments.

It is however important to highlight that mass shift is not the only consequence of sample topology. Independently of the instrument used, the thickness of the sample also affects

**Table 2** Effect of the surface topology of imaged agar samples using mass spectrometry on the experimental mass shift (reference mass = theoretical mass of polyethylene oxide methyl ether (PEO) $[PEO17+Na]^+$ ($m/z$ = 803.4616). MALDI ToF was a rapifleX and the MALDI FT-ICR was a solariX XR 9.4T. Thicknesses of the PEO embedded in agar were ranged as T4 > T3 > T2 > T1. See ESM Fig. S1

| Mass analyzers | | Sample height of agar sample containing polyethylene oxide methyl ether (T4 > T3 > T2 > T1) | | | | | | | |
|---|---|---|---|---|---|---|---|---|---|
| | | TIC (cps) | | | | Mass shift (ppm) | | | |
| | | T1 | T2 | T3 | T4 | T1 | T2 | T3 | T4 |
| ToF | Average | 792 | 695 | 441 | 332 | 0.00 | −58.02 | −256.20 | −374.80 |
| | Standard deviation | ± 10 | ± 9 | ± 6 | ± 5 | ± 1.29 | ±1.4 | ± 1.9 | ± 1.8 |
| FT-ICR | Average | $7.40\times10^7$ | $7.32\times10^7$ | $6.81\times10^7$ | $7.42\times10^7$ | 0.00 | −0.06 | 0.41 | 0.5 |
| | Standard deviation | $\pm3.32\times10^5$ | $\pm2.45\times10^5$ | $\pm3.62\times10^5$ | $\pm3.24\times10^5$ | ± 0.05 | ± 0.05 | ± 0.02 | ± 0.01 |

the signal intensity. Indeed, the sample surface is no longer in the focal plane of the laser, a reduction of the photon density occurs resulting in a decrease of the apparent ionization efficiency. This loss of sensibility could eventually be mitigated by increasing the laser energy above the threshold energy required for the sample ionization [28]. An uneven surface can also cause a loss in lateral resolution, as the laser ablation spot size may be modified. Up to now, there is no commercially available MALDI source with a pixel to pixel autofocus, but the Spengler group has shown in 2017 that images on irregular surfaces can be achieved without height-related signal artifacts by adjusting sample stage's *z*-position based on a topographic image of the sample [29].

In Fig. 2, we are presenting the heatmaps of the mass shift from a lipid ion at *m/z* 828.5514 (putatively identified as [PC 38:6+Na]$^+$ according to Lipid MAPS LSMD) present in a non-flat sample (beveled slice of salmon brain homogenate, depicted "beveled" sample as shown in Fig. 2a) and a flat sample (flat slice of salmon brain homogenate, depicted "flat" sample in Fig. 2b) acquired on the rapifleX (MALDI ToF) and the solariX XR (MALDI FT-ICR). The *m/z* distribution of this ion is free of isobaric interferences in both MS instrument. The mass shifts have been calculated according to Eq. 1 using the exact mass of this lipid (*m/z* = 828.5514). In the MALDI ToF data, the "flat" sample shows a rather stable mass shift (Fig. 2f); however, the mass shift calculated from the "beveled" sample (Fig. 2d) is shown to be greater in the pixels located at the lower height of the "beveled" sample (mass shift was estimated at +180 ppm). In the FT-ICR MS data, the mass shift remains below 2 ppm and shows no correlation with sample height. These results demonstrate that flat samples are required for accurate MSI data acquisition involving

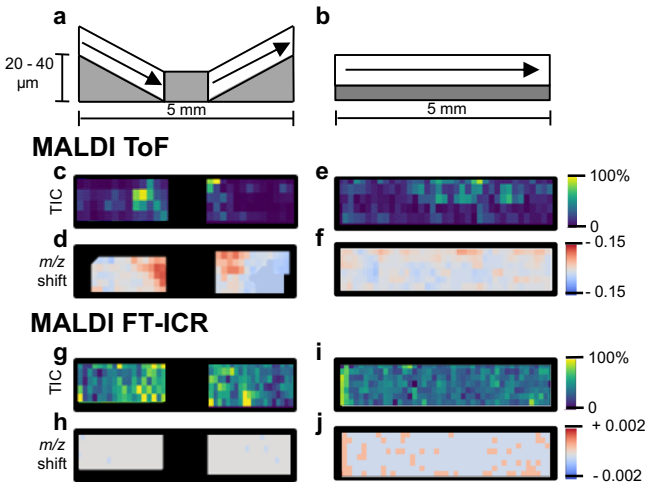


**Fig. 2** Beveled (a) and flat (b) samples topographies representation. TIC heatmap for ToF ((c) for "beveled" and (e) for "flat" samples) and FT-ICR ((g) for "beveled" and (i) for "flat" samples) acquisitions. Mass shift heatmaps for *m/z* 828.5514 in ToF ((d) for "beveled" and (f) for "flat" samples) and FT-ICR ((h) for "beveled" and (j) for "flat" samples) MSI data

MALDI ToF, especially when the MALDI source is coupled with a linear ToF mass analyzer. Alternatively, the surface topology contribution is less critical for FT-ICR instrument, which ensures a limited variation of the TIC variation from one pixel to another.

In some cases, sample flatness is not enough to prevent mass shift occurring. Indeed, the mode of matrix deposition affects the homogeneity of the matrix crystals [30, 31] and may induce mass shift as well. As previously shown in Fig. 1a, the heterogeneity of the matrix crystals can induce a significant mass shift for the signal of [Lactosyl C12 ceramide + Na]$^+$ acquired on a MALDI ToF. This mass shift could result from topology variation caused by a heterogeneous distribution of crystals of different sizes and thicknesses. Considering individual spectra of selected pixels, the importance of the mass shift mainly depends on the crystal morphology on the sample (Fig. 3a). In order to investigate the effect of the matrix crystal size on the mass shift, we considered additional matrix deposition methods, such as spraying the matrix on the sample using the HTX sprayer (Fig. 3b) or matrix sublimation using the HTX Sublimator (Fig. 3c). Images obtained by electron and inverted optical microscopy of these samples (see ESM Fig. S2) show improved crystal formation and homogeneity of the matrix deposition under these two matrix deposition techniques. MS peaks extracted from several randomly selected pixels show the reduction of mass shift. Compared to the dried droplet method, matrix sublimation and, to a lesser extent, HTX matrix spraying resulted in better mass resolving power in the average spectrum by reducing the mass shift from one pixel to another.

Nonetheless, the calculated mass accuracy from the peak apex of [Lactosyl C12 ceramide + Na]$^+$ (*m/z* = 828.5444) in the average spectrum is still relatively low (mass errors are estimated at 100 ppm, − 170 ppm, and − 300 ppm in Fig. 3a, b, and c respectively). Since each image was independently and externally calibrated from red phosphorus, these mass errors suggest differences in topology (*Z*-axis) between the calibrating substance and the sample surface.

Interestingly, the crystal heterogeneity could also influence the MS peak width within a single pixel (Fig. 3a, pixels depicted 6, 7, 8, 9, and 10). As the loss in mass resolving power has already occurred at the pixel level, the mass resolving power in the average MS spectrum is inherently affected. In ToF instruments, several MS spectra are cumulated to generate the MS spectrum recorded for the pixel position. In other words, MS spectra recorded in each pixel is already a combination of several MS scans. As a consequence, the MS peak widening due to mass shift can also be observed in a pixel spectrum, as it is the case here. This observation can be explained by (i) the micro-heterogeneity sampled by the laser beam and/or (ii) the crystal morphology changes due to the successive laser ablations [32–34], and tend to be less

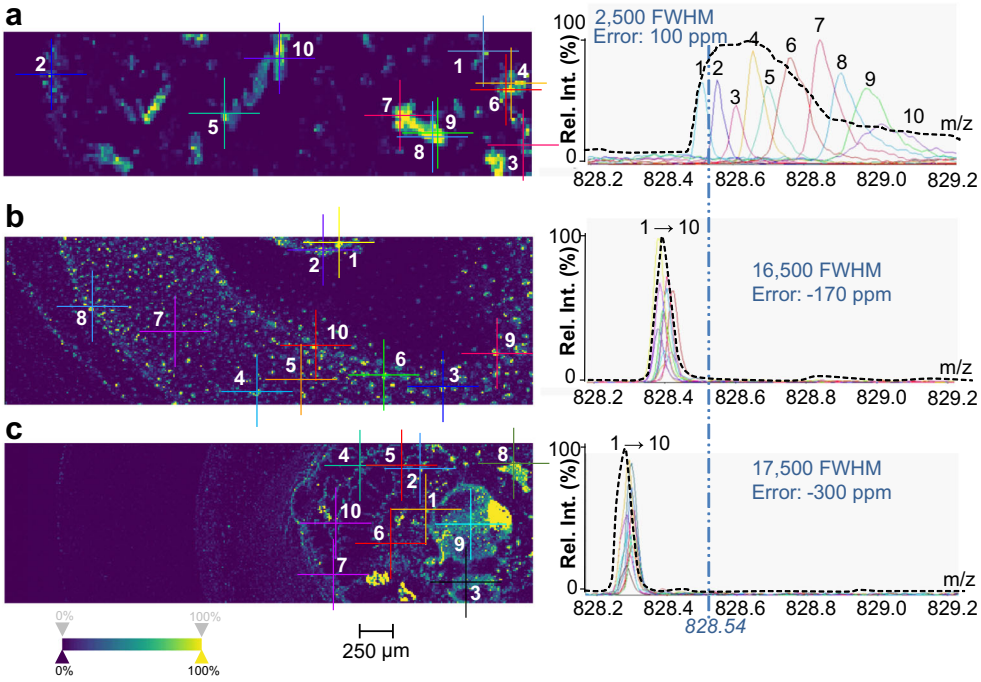


**Fig. 3** [Lactosyl C12 ceramide + Na]$^+$ (theoretical $m/z$ = 828.5444) mass spectrometry images acquired with the rapifleX MALDI ToF instrument using different DHB matrix deposition processes. **a** Dried droplet method, **b** HTX Sprayer, **c** HTX Sublimator. Color-coded crosses on the heatmaps correspond to their different individual spectrum at the right of the ion intensities heatmaps. Black dashed line represents the [Lactosyl C12 ceramide + Na]$^+$ distribution in MSI average spectrum. The theoretical $m/z$ value of [Lactosyl C12 ceramide + Na]$^+$ is represented by a blue vertical dashed line. Each image acquisition was externally and independently calibrated using red phosphorus spots

significant in samples with homogeneous crystallization (Fig. 3b and c). These observations suggest that MS peak broadening can occur in parallel to MS peak shifting in MALDI ToF instrument during the MSI acquisition due to the laser ablation of the matrix. MS peak widening in a single pixel was not observed in FT-ICR instrument since only one MS acquisition is performed for each pixel. A peak width monitoring on each pixel could be performed to highlight crystal morphology variations and/or micro-heterogeneities at the pixel scale.

## Mass shift prevention

### Considerations for performing a robust MS calibration for MSI analyses

Mass shift is related, inter alia, to the sample composition (affecting the space charge effect) and to the sample surface topology. Since these sample properties directly influence the physical quantities measured by the MS instrument, it is recommended to calibrate the instrument with calibrating substances in similar experimental conditions to the sample wherever possible [35, 36]. The MS calibration of heterogeneous MSI samples is thus quite challenging since the sample composition and local heterogeneity is not known before performing the mass spectrometry images of the current sample. Pre-acquisition of a similar sample, such as adjacent or contiguous tissue section, would appear to be promising but there is no guarantee that the mass spectrometry image of this sample will provide a correct external calibration of the target sample. Theoretically one can consider implementing as many external calibration points as required to fit the local properties of the imaged sample at the pixel scale. From a practical point of view, this would be almost impossible to achieve and extremely time-consuming and would probably increase the risk of miss calibrating the MSI data. A workaround would be to apply an internal MS calibration by adding calibrating substances or using some known signal of the sample. Attempts may be made to use matrix ions as calibrating points but this would lead to poor calibration due to the lack of a mass range covering. It is also possible to use the sample signals as an internal MS calibration, such as the sample lipid signals [37], but this would require knowing the sample composition in advance. On the other hand, the addition of a calibrating substance to the sample can increase the competition for ionization between the calibrating compounds and the intrinsic molecules of the sample to be imaged by mass spectrometry. Worse yet, this competition between the calibrating compounds and the molecules from the sample is expected to vary from pixel to pixel, making the MSI interpretation impossible. In the absence of an internal standard, a correct MS calibration should be performed with the same acquisition parameters as the sample to obtain signals with comparable intensities, and at the same sample height.

### Mass shift prevention due to unstable TIC

As previously shown, mass shift depends on several imaging parameters and is not constant from one pixel to another. It is however possible to restrain the mass shift even in complex samples by astutely tuning the acquisition parameters of the instrument, especially the MALDI source parameters.

Bacterial-interaction samples are well suited to highlight sample composition and topology variation effects on mass accuracy.

To this end and for each experiment, mass shift and peak widths were calculated using the mycosubtilin ion $[C_{49}H_{76}N_{12}O_{14}+Na]^+$, $m/z$ = 1079.5496 as the reference ion, and presented as a heatmap in Fig. 4, thanks to our visualization software.

The images acquired on the ToF instrument show a similar mass shift, independently of the number of laser shots applied (2000 laser shots Fig. 4a and 20 laser shots Fig. 4b). Mass shift varies from −200 to +200 ppm, and appears to be superimposed with the bacterial colonies localization. On both colonies (e.g., *Bacillus velezensis GA1* and *Pseudomonas Sp. CMR12a*), where the sample is expected to be the thickest, a negative mass shift of −200 ppm is observed, in compliance with the data obtained from the various PEO embedded agar thicknesses and the brain homogenate samples. Peak width distribution is also relatively similar between these two data (Fig. 4f, g), by showing larger peak width in *Pseudomonas Sp. CMR12a* near environment. This increasing peak width in this specific region would suggest the presence of inhomogeneous matrix crystals, potentially reflecting the sample heterogeneity.

The mass shift observed in the FT-ICR data ranges from 0 to 50 ppm and appears to be correlated with the laser shots number. When using 2000 laser shots per pixel, a mass shift around 50 ppm was observed (Fig. 4c), which deviates considerably from the manufacturer's specification (± 0.5 ppm). By reducing the number of laser shots (Fig. 4d and e), the TIC was stabilized and the space charge effect became negligible. As a result, the mass shift was drastically reduced, until approaching the variation of about ± 0.5 ppm. Reducing the number of laser shots thereby demonstrate significant improvements regarding the mass shift. On the FT-ICR images, the selected reference ion is visible on every pixel of the image in the MSI data acquired with 2000 laser shots (Fig. 4c and h). When decreasing the laser shots number, the reference ion signal appears to be suppressed below the limit of detection, and is no longer visible for some pixels, left in blank on the image (see *Pseudomonas SP. CMR12a* area, Fig. 4e and j). The peak width distribution on the FT-ICR image does however remain constant (Fig. 4h, i, and j) as expected for this instrument where only one MS scan is performed per pixel.

These results show that mass shift effects are present on both ToF and FT-ICR instruments, but with different origins (either sample topology or space charge effect variations for ToF or FT-ICR analyzers respectively). However, mass shift seems to be controlled under a fine-tuning of the acquisition parameters on the FT-ICR instrument [38]. Our recommendation for FT-ICR analyzers is then to optimize the MALDI source settings to stabilize the amount of ion injected to the mass analyzer in order to limit the space charge effect during the $m/z$ determination. This optimization will be performed according to the type and the specification of the mass analyzers (ToF, type of ICR cell

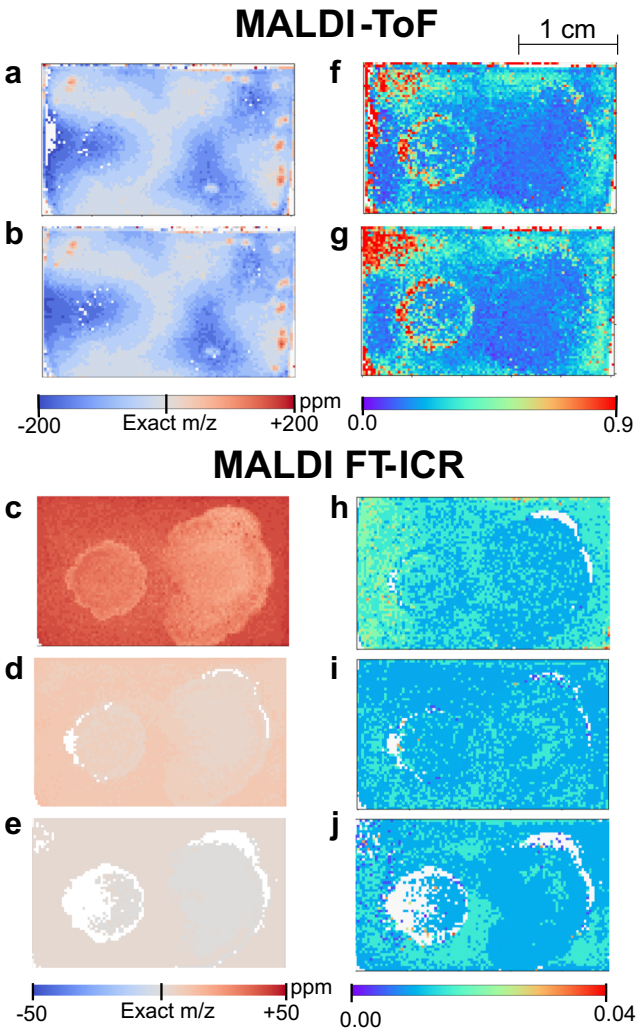


**Fig. 4** Heatmaps of mass shifts (a, b, c, d, and e) and peak distribution widths (f, g, h, i, and j) for MSI of a co-culture of *Bacillus velezensis GA1* and *Pseudomonas sp. CMR12a*, using the mycosubtilin ion $[C_{49}H_{76}N_{12}O_{14}+Na]^+$, $m/z$ = 1079.5496 as the $m/z$ of reference. Images were acquired on a rapifleX MALDI ToF using 2000 shots (a and f) or using 20 shots (b and g) and on a solariX XR MALDI FT-ICR using 2000 shots (c and h), 200 shots (d and i), or 20 shots (e and j). The pixels where the ion $m/z$ = 1079.5496 was not detected are left in blank

and power of the supra-conducting magnet FT-ICR, or any other critical specification of the instrument used for mass spectrometry imaging), and by monitoring the signal-to-noise ratio to avoid any loss of signal of interest.

### Mass shift prevention due to heterogeneous sample topology

As discussed in the mass shift understanding section, topology variation is the main factor influencing mass shift in linear TOF instruments. Limiting the topology variation should therefore be considered to increase the accuracy and the resolution of MSI analyses with these instruments. When possible, sample preparation should ensure flat samples (as illustrated in Fig. 2). If available, stage tilt correction should also be

performed before acquisition to avoid sample height variation due to misalignment of the sample [16]. As illustrated above, a homogenous matrix deposition technique is also recommended to avoid sample topology variation caused by the matrix layer. For not flat samples (i.e., when sample topology variations cannot be reduced), sample topology variation can be compensated by acquisition strategies involving source settings adaptation to the sample height (e.g., pixel to pixel autofocus) [29]. As a last resort, the use of TOF instruments with orthogonal source (i.e., reduced kinetic energy dispersion) or trap instrument (e.g., Orbitrap, FT-ICR) could be considered since the sample topology does not influence the *m/z* measurement on these devices.

## Mass shift reduction by data post processing

Mass shift amplitude in MSI data can be controlled through sample preparation and acquisition parameters optimization. When these recommendations cannot be met, post-processing methods can be applied (i) to mitigate mass shifts effects (data realignment or data recalibration) and (ii) to correct a low mass accuracy (data recalibration).

Mass spectra realignment allows comparison of all spectra contained in an MSI dataset and uses statistical tools to reassemble shifted *m/z* values to a unique value. However, this unique *m/z* value can significantly differ from the accurate *m/z* value of the ion if the initial calibration is not correct. Diversely, mass spectra recalibration will recalibrate the data based on specific signals from the sample [39, 40], resulting in a diminution of mass shifts between pixels and an improvement of the mass accuracy. However, recalibration methods depend on specific signals and experimental conditions applied to the sample (e.g., use of Ag or Au particles, rich peptide signals, *m/z* peak annotation assumption based on the state of the art) and are not applicable to the majority of MSI experiments. Recently, a new method developed by La Rocca et al. [22] introduced a more versatile approach to recalibrate MSI data based on mass shift estimation. This is applicable to different mass analyzers and on different samples with a specific focus on lipid and metabolite signals. This approach aims to recalibrate each pixel individually based on a list of potential internal calibrants generated from other annotated MSI data or databases.

In this section, we have applied this recalibration algorithm on three MSI data of bacteria co-culture obtained with different acquisition conditions on the MALDI FT-ICR (see Fig. 5c, e, and g, using 2000, 200, and 20 laser shots respectively) and on the MALDI TOF (see Fig. 5a using 20 laser shots). Applied recalibration parameters are detailed in the ESM. A minimum of 10 matches (between experimental signals and calibrating ion lists) per pixel was set to properly recalibrate the pixel correctly. Below 10 matches, the pixel is not recalibrated and removed

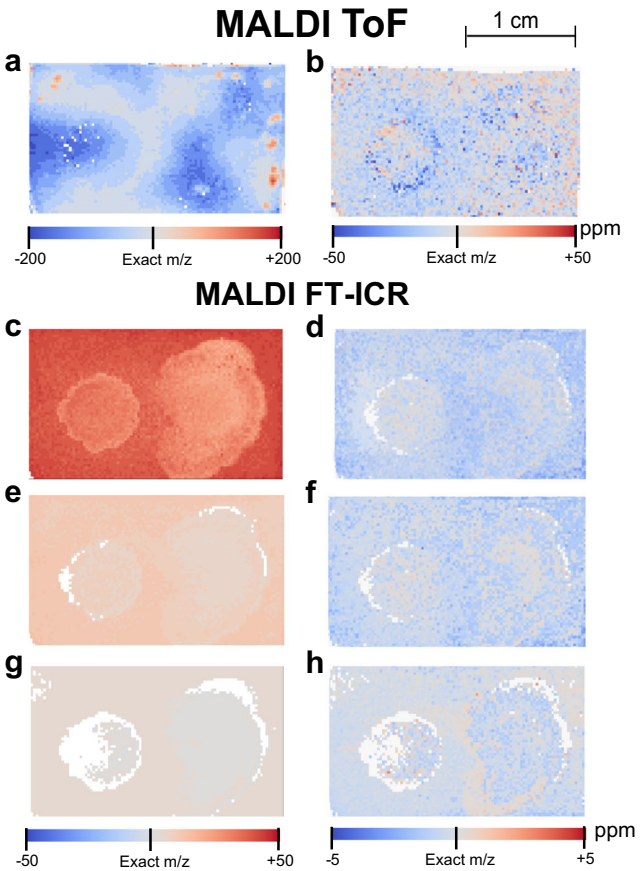


**Fig. 5** Comparison of mass shift heatmaps. The figures to the left are the RAW MSI data and to the right the post-reprocessed (realignment + recalibration) MSI data. Mass shifts were calculated using the ion of mycosubtilin as a reference ($[C_{49}H_{76}N_{12}O_{14}+Na]^+$ (*m/z* = 1079.5496). **a** and **b** correspond to the original and recalibrated MALDI ToF data respectively. MALDI FT-ICR MSI data acquired with different source settings, **c** and **d** are for the original and recalibrated data using 2000 laser shots respectively, **e** and **f** are for the original and recalibrated data using 200 laser shots respectively, and g and h are for the original and recalibrated data using 20 laser shots respectively). All pixels where a minimum of 10 matches for the recalibration was not reached or where the ion *m/z* = 1079.5496 was not detected were left in blank

from the MSI data (represented with blank pixels in a reconstructed image).

The mass shift comparison of the original data to the recalibrated MSI data in Fig. 5 allows the investigation of the algorithm performance to reduce the mass shift in function of the initial quality of the MSI data. The recalibration performance was estimated by the percentage of pixels where the measured mass shift was below 1 ppm, 3 ppm, and 5 ppm for the FT-ICR instrument and below 10 ppm, 15 ppm, and 20 ppm for the ToF instrument as shown in Table 3, according to the theoretical mass from our local lipopeptides database. Before recalibration by our software, extreme values of mass shift rose up to ± 50 ppm for FT-ICR when a higher number of laser shots was set (Fig. 5c). This significant mass shift was reduced by decreasing the number of laser shots (Fig. 5e and g).

**Table 3** Percentage of pixels with mass accuracy below 1, 3, and 5 ppm for MSI data acquired with MALDI ToF (rapifleX) and MALDI FT-ICR (solariX XR) and below 10, 15, and 20 ppm uniquely for ToF MSI (rapifleX). The errors were computed with the theoretical *m/z* 1079.5496 from mycosubtilin for bacteria co-culture experiments and with *m/z* 828.5514 (PC 38:6) for salmon brain homogenate experiments

| | Original MSI data | | | | Recalibrated MSI data | | | |
|---|---|---|---|---|---|---|---|---|
| **MALDI FT-ICR** | **< 5 ppm** | **< 2 ppm** | **< 1 ppm** | **< 0.5 ppm** | **< 5 ppm** | **< 3 ppm** | **< 1 ppm** | **< 0.5 ppm** |
| Bacteria 2000 laser shots | 0.00 | 0.00 | 0.00 | **0.00** | 100.00 | 91.81 | 24.81 | 10.53 |
| Bacteria 200 laser shots | 0.14 | 0.14 | 0.00 | 0.00 | 100.00 | 99.98 | 69.03 | 37.21 |
| Bacteria 20 laser shots | 100.00 | 31.49 | 27.11 | 8.00 | 99.98 | 99.98 | 88.01 | 65.38 |
| Homogenate "Beveled" | 100.00 | 94.06 | 90.50 | 0.00 | 100.00 | 100.00 | 94.06 | 84.16 |
| Homogenate "Flat" | 100.00 | 98.34 | 75.93 | 0.28 | 100.00 | 100.00 | 100.00 | 75.52 |
| **MALDI ToF** | **< 20 ppm** | **< 15 ppm** | **< 10 ppm** | **< 5 ppm** | **< 20 ppm** | **< 15 ppm** | **< 10 ppm** | **< 5 ppm** |
| Bacteria 2000 laser shots | 25.42 | 0.00 | 0.00 | 0.00 | 92.03 | 84.21 | 66.08 | 36.01 |
| Bacteria 20 laser shots | 25.65 | 0.00 | 0.00 | **0.00** | 92.90 | 84.61 | 66.16 | 36.01 |
| Homogenate "Bevel" | 2.40 | 2.40 | 0.48 | 0.48 | 46.42 | 45.66 | 23.02 | 12.01 |
| Homogenate "Flat" | 0.67 | 0.67 | 0.00 | 0.00 | 98.50 | 94.67 | 79.00 | 44.33 |

The acquisition of the same sample in the ToF instrument showed that mass shift reached up to ± 200 ppm (Fig. 5a). After the application of the recalibration algorithm, the extreme values of mass shift were reduced to ± 5 ppm for the three MSI data acquired on the FT-ICR instrument (Fig. 5d, f, and h). The mass shift was reduced to below 1 ppm for 80% of the pixels after recalibration when using the optimized MALDI source settings with 20 laser shots. For the ToF instrument, the recalibration led to mass shifts below 15 ppm for 80% of the pixels, a fair improvement over the initial 200 ppm obtained in the MSI raw dataset. This significant improvement of the post-processing distribution is provided in Fig. 5d, f, and h. Overall and independently of the selected instrument, the smaller the initial mass shift, the better the recalibration efficiency. Nonetheless, it is important to highlight that the number of non-recalibrated pixels is higher when the laser shots are low, potentially due to a signal drop below the limit of detection. Consequently, a compromise can now be found between an acceptable mass shift (improved number of annotated peaks) and an acceptable ionization efficiency (improved number of detected peaks) in mass spectrometry imaging experiments. The same conclusions were obtained on the salmon brain homogenate (see ESM Fig. S3 and Table S1)

These results strongly support the effectiveness of the data recalibration to reduce the mass shift effect since all recalibrated MSI data exhibit smaller mass shift than original data. However, the performance of this algorithm depends on the initial quality of the MSI data. Consequently, it is recommended to control the mass shift at every step of the MSI workflow to ensure the best MSI post-processing recalibration. Furthermore, it is important to maintain sufficient signals to perform the recalibration of the whole MSI data.

This additional gain in accuracy after data recalibration has also been supported by the drastic increase of annotation (compound identification) on METASPACE [41] after data recalibration for all the investigated MSI data (see ESM Fig. S4).

## Application MSI suggested workflow

Based on our results and on the literature, best quality MSI data with a controlled mass shift can be obtained when following the recommendations summarized in Table 4.

We applied this workflow to a mouse brain tissue section to show the quality of mass spectrometry images that can now be

**Table 4** General recommendations for mass shift visualization, diagnostic, and reduction according to the type of instrument

| Type of instrument | Mass shift sources | Mass shift visualization and diagnostic | Mass shift reduction/correction strategy |
|---|---|---|---|
| FT-ICR | Sample heterogeneity | Mass shift is correlated to the total ion count (TIC) | TIC should be monitored (e.g., reducing laser shots number or applying automatic gain control) |
| TOF | Sample thickness variation | Mass shift is correlated to sample topology | Sample flatness verification<br>Stage tilt correction<br>Source settings adaptations pixel by pixel (if possible) |
| | Inhomogeneous matrix deposition | Pixels peak width increases | Matrix deposition should be optimized |

**Table 5** Mass accuracies of the two monitored lipids (*m/z* 739.4675 identified as PA 36:2+$K^+$ and 838.6164 identified as HexCer 40:1;O3+$K^+$) during the mass spectrometry imaging of mouse tissue section showed in Fig. 6 acquired on a solariX XR 9.4T MALDI FT-ICR before and after post-processing recalibration using our in-house software

| | Original RAW MSI data | | | | | | Post-processing recalibrated MSI data | | | | | |
|---|---|---|---|---|---|---|---|---|---|---|---|---|
| Mass accuracy (ppm) | > 5 | > 2 | > 1 | > 0.75 | > **0.5** | > 0.25 | > 5 | > 2 | > 1 | > 0.75 | > **0.5** | > 0.25 |
| *m/z* | Percentage of pixels where the detected ions get a mass accuracy better than the specified range[a] | | | | | | | | | | | |
| **739.4675** | 99.61 | 87.70 | 82.49 | 14.70 | 14.70 | 0.00 | 100.00 | 100.00 | 99.98 | 96.40 | 83.41 | 49.15 |
| **838.6164** | 100.00 | 96.91 | 14.54 | 14.54 | 14.54 | 0.00 | 100.00 | 99.84 | 99.39 | 86.37 | 83.25 | 55.86 |

[a] Pixels where the ions were not detected are excluded for the percentage calculation

**0.5 ppm** is the mass accuracy specification of the solariX XR FT-ICR according to the manufacturer in normal operation

routinely achieved with the solariX XR 9.4T mass spectrometers. Table 5 shows the percentage of pixels in different ranges of mass accuracies (from 0.25 to more than 5 ppm). Two lipid ions, PA 36:2 with a potassium adduct ($C_{39}H_{73}O_8K$, *m/z* = 739.4675) and HexCer 40:1;O3 ($C_{46}H_{89}NO_9K$, *m/z* = 838.6164) were monitored to illustrate this purpose. These ions have been identified thanks to the high mass accuracy achieved throughout the entire image and the contribution of the isotopic fine structure obtained by the dynamically harmonized ICR cell of the solariX XR (see ESM Figs. S5 and S6). The ions show a different distribution in the mouse brain tissue (Fig. 6b and c for [PA 36:2+K]$^+$ and [HexCer 40:1;O3+K]$^+$ respectively). However, their calculated mass shift is not related to their distribution (Fig. 6d and e for [PA 36:2+K]$^+$ and [HexCer 40:1;O3+K]$^+$ respectively), but to the areas where the TIC is the highest (Fig. 6a, corresponding to the fiber tracts region). As reported in Table 5, the [PA 36:2+K]$^+$ ion, mainly distributed in the low shifted regions (i.e., where the TIC is low), has more than 80% of its pixels with an accuracy better than 1 ppm before recalibration process. Diversely, the ion [HexCer 40:1;O3+K]$^+$, mainly distributed in the high shifted regions (i.e., where the TIC is high), presents less than 15% of its pixels with an accuracy better than 1 ppm. After the recalibration method, more than 80% of the pixels show a mass accuracy better than 0.5 ppm, and the mass shift distribution no longer corresponds to the TIC for both lipids (Fig. 6f and g for [PA 36:2+K]$^+$ and [HexCer 40:1;O3+K]$^+$ respectively).

## Conclusion

This study presented a critical analysis of experimental parameters allowing a significant reduction of the mass shift occurring in MSI analysis. The workflow was optimized on two types of instruments commonly used in MALDI MSI (i.e.,

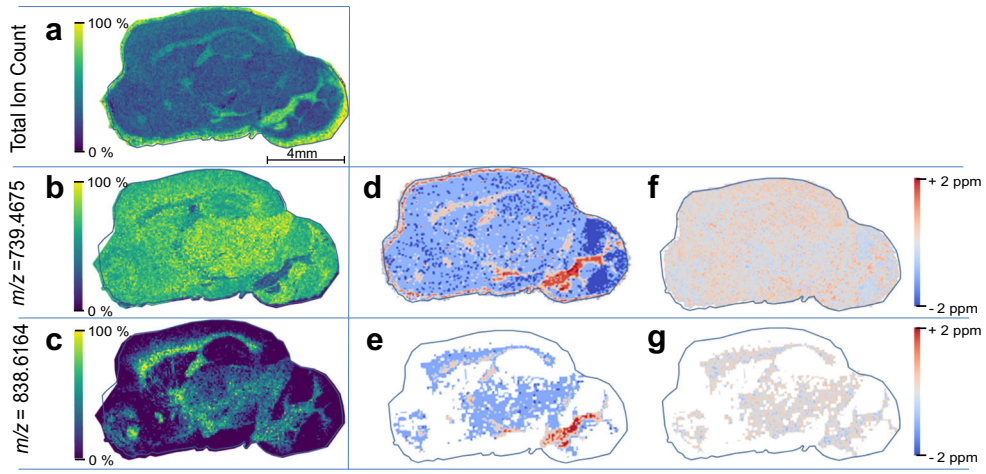


**Fig. 6** Mass spectrometry imaging of mouse tissue section acquired on a solariX XR 9.4T MALDI FT-ICR using our recommended optimized workflow (i.e., flat tissue section, homogeneous HCCA matrix deposition, 20 laser shots par pixel for TIC (total ion current) stabilization) at nominal resolving power FWHM higher than 220,000 at *m/z* 800. **a** is the image of the TIC. **b** and **c** depict mass spectrometry images of [PA 36:2+K]$^+$ and [HexCer 40:1;O3+K]$^+$ respectively (black pixel in (**c**) corresponds to pixel where [HexCer 40:1;O3+K]$^+$ is not detected). **d** and **f** depict mass shifts heatmaps of [PA 36:2+K]$^+$before and after post-processing recalibration respectively. **e** and **g** are the mass shifts heatmaps of [HexCer 40:1;O3+K]$^+$ before and after post-processing recalibration respectively

rapifleX and solariX XR 9.4T from Bruker) but could be extended to others. The narrowing of the *m/z* distribution, thanks to mass shift reduction coupled with internal recalibration, allowed a better mapping of compounds and enabled more confident signal annotations. The origins of mass shift can differ from one MS instrument to another. In the MALDI ToF instrument, the sample topology directly influences the kinetic energy given to the ions leading to *m/z* measurement deviations. We reported that the sample preparation can be optimized (i.e., improving the sample flatness and the homogeneity of the matrix deposition) to reduce mass shift. The main factor influencing mass shift in FT-ICR is the variation of the total ion current (TIC) leading to Coulomb expansion of the ion cloud in the FT-ICR cell. Maintaining the TIC values below a given value and therefore avoiding Coulomb expansion during the acquisition facilitates the drastic reduction of the mass shift in these MS instruments. The optimization of the sample preparation and the MS instrument parameters can easily be applied in general MSI workflow.

Whenever possible, the use of orthogonal sources for TOF instruments (i.e., reducing the kinetic energy dispersion) and automatic gain control for FT-ICR-MS instruments (i.e., controlling the ions injected in the FT-ICR cell) are also highly recommended to minimize mass shift in MSI. Meta-analysis of data by bio-informatic tools suggests indeed that Orbitrap should be less impacted by the mass shift [22]. However, the metadata of the acquisition methods are still scarce and the MSI parameter influences on mass shift remain to be investigated. Recent data obtained in our lab on biological sample obtained on a MALDI ion mobility ToF (unpublished results obtained on timstof FleX prototype, Bruker, Bremen, Germany) strongly suggest that the effect of surface topology on mass shifts is negligible since the kinetic energy dispersion practically no longer exists after the ion mobility section of the instrument.

**Supplementary Information** The online version contains supplementary material available at https://doi.org/10.1007/s00216-021-03174-1.

**Acknowledgments** The authors would like to thank the University of Maastricht (The Netherlands) and Dr. S. Ellis for the use of the HTX Sprayer and the HTX Sublimator, Pr. M. Ongena and Dr. A. Argüelles Arias, Microbial Processes and Interactions (MiPI) of Gembloux Agro Biotech (Belgium), for the bacteria samples. D. Van Kruining and Pr. P. Martinez Martinez, Department of Psychiatry and Neuropsychology, School for Mental Health and Neuroscience, Maastricht University (The Netherlands), are kindly acknowledged for providing the mouse brain tissue samples. CAREM platform (University of Liège, Belgium) is thanked for performing electron microscopy acquisition of the crystal samples.

**Funding** This work was funded by the Excellence Of Science Program, FNRS F.R.S (Rhizoclip EOS30650350), by the European Union Horizon 2020 research and innovation program under grant agreement No. 731077 and by interreg's EURLIPIDS project (R-8598). The MALDI ToF RapifleX and the MALDI FT-ICR SolariX XR were funded by FEDER BIOMED HUB Technology Support (number 2.2.1/996).

## Compliance with ethical standards

All experiments were done with permission of the Committee on Animal Welfare, Maastricht University, according to Dutch governmental rules.

**Conflict of interest** The authors declare that they have no conflict of interest.

## References

1. Amstalden van Hove ER, Smith DF, Heeren RM. A concise review of mass spectrometry imaging. J Chromatogr A. 2010;1217(25):3946–54. https://doi.org/10.1016/j.chroma.2010.01.033.
2. Luxembourg SL, Mize TH, McDonnell LA, Heeren RMA. High-spatial resolution mass spectrometric imaging of peptide and protein distributions on a surface. Anal Chem. 2004;76(18):5339–44. https://doi.org/10.1021/ac049692q.
3. Caprioli RM, Farmer TB, Gile J. Molecular imaging of biological samples: localization of peptides and proteins using MALDI-TOF MS. AnalChem. 1997;69(23):4751–60. https://doi.org/10.1021/ac970888i.
4. Kune C, McCann A, La Rocca R, Arias AA, Tiquet M, Van Kruining D, et al. Rapid visualization of chemically related compounds using Kendrick mass defect as a filter in mass spectrometry imaging. Anal Chem. 2019;91(20):13112–8. https://doi.org/10.1021/acs.analchem.9b03333.
5. Brown SC, Kruppa G, Dasseux JL. Metabolomics applications of FT-ICR mass spectrometry. Mass Spectrom Rev. 2005;24(2):223–31. https://doi.org/10.1002/mas.20011.
6. McLafferty FW. Tandem mass spectrometry. Science. 1981;214(4518):280–7. https://doi.org/10.1126/science.7280693.
7. de Hoffmann E. Tandem mass spectrometry: a primer. J Mass Spectrom. 1996;31(2):129–37. https://doi.org/10.1002/(sici)1096-9888(199602)31:2<129::Aid-jms305>3.0.Co;2-t.
8. Griffiths WJ, Jonsson AP, Liu S, Rai DK, Wang Y. Electrospray and tandem mass spectrometry in biochemistry. Biochem J. 2001;355(Pt 3):545–61. https://doi.org/10.1042/bj3550545.
9. Kanu AB, Dwivedi P, Tam M, Matz L, Hill HH Jr. Ion mobility–mass spectrometry. J Mass Spectrom. 2008;43(1):1–22. https://doi.org/10.1002/jms.1383.
10. Lanucara F, Holman SW, Gray CJ, Eyers CE. The power of ion mobility-mass spectrometry for structural characterization and the study of conformational dynamics. Nature Chemistry. 2014;6(4):281-94. https://doi.org/10.1038/nchem.1889
11. Lapthorn C, Pullen F, Chowdhry BZ. Ion mobility spectrometry-mass spectrometry (IMS-MS) of small molecules: separating and assigning structures to ions. Mass Spectrom Rev. 2013;32(1):43–71. https://doi.org/10.1002/mas.21349.
12. Gorshkov MV, Nikolaev EN. Optimal cyclotron radius for high resolution FT-ICR spectrometry. Int J Mass Spectrom Ion Process. 1993;125(1):1–8. https://doi.org/10.1016/0168-1176(93)80012-4.
13. Easterling ML, Mize TH, Amster IJ. Routine part-per-million mass accuracy for high- mass ions: space-charge effects in MALDI FT-ICR. Anal Chem. 1999;71(3):624–32. https://doi.org/10.1021/ac980690d.
14. Nikolaev EN, Kostyukevich YI, Vladimirov GN. Fourier transform ion cyclotron resonance (FT ICR) mass spectrometry: theory and simulations. Mass Spectrom Rev. 2016;35(2):219–58. https://doi.org/10.1002/mas.21422.
15. Phelan VV, Liu WT, Pogliano K, Dorrestein PC. Microbial metabolic exchange–the chemotype-to-phenotype link. Nat Chem Biol. 2012;8:26.

16. Malys BJ, Piotrowski ML, Owens KG. Diagnosing and correcting mass accuracy and signal intensity error due to initial ion position variations in a MALDI TOFMS. J Am Soc Mass Spectrom. 2018;29(2):422–34. https://doi.org/10.1021/jasms.8b05757.
17. Berghmans E, Van Raemdonck G, Schildermans K, Willems H, Boonen K, Maes E, et al. MALDI mass spectrometry imaging linked with top-down proteomics as a tool to study the non-small-cell lung cancer tumor microenvironment. Methods Protoc. 2019;2(2):44. https://doi.org/10.3390/mps2020044.
18. Gemperline E, Chen B, Li L. Challenges and recent advances in mass spectrometric imaging of neurotransmitters. Bioanalysis. 2014;6(4):525–40. https://doi.org/10.4155/bio.13.341.
19. McDonnell LA, Heeren RMA. Imaging mass spectrometry. Mass Spectrom Rev. 2007;26(4):606–43. https://doi.org/10.1002/mas.20124.
20. Nihorimbere V, Cawoy H, Seyer A, Brunelle A, Thonart P, Ongena M. Impact of rhizosphere factors on cyclic lipopeptide signature from the plant beneficial strain Bacillus amyloliquefaciens S499. FEMS Microbiol Ecol. 2012;79(1):176–91. https://doi.org/10.1111/j.1574-6941.2011.01208.x.
21. Debois D, Ongena M, Cawoy H, De Pauw E. MALDI-FTICR MS imaging as a powerful tool to identify Paenibacillus antibiotics involved in the inhibition of plant pathogens. J Am Soc Mass Spectrom. 2013;24(8):1202–13. https://doi.org/10.1007/s13361-013-0620-2.
22. La Rocca R, Kune C, Tiquet M, Stuart L, Alexandrov T, De Pauw E, et al. Using biological signals for mass recalibration of mass spectrometry imaging data. ChemRxIv. 2020. https://doi.org/10.26434/chemrxiv.12901679.v1.
23. Sud M, Fahy E, Cotter D, Brown A, Dennis EA, Glass CK, et al. LMSD: LIPID MAPS structure database. Nucleic Acids Res. 2007;35(Database issue):D527–32. https://doi.org/10.1093/nar/gkl838.
24. Ievlev AV, Belianinov A, Jesse S, Allison DP, Doktycz MJ, Retterer ST, et al. Automated interpretation and extraction of topographic information from time of flight secondary ion mass spectrometry data. Sci Rep. 2017;7(1):17099. https://doi.org/10.1038/s41598-017-17049-y.
25. Yang JY, Phelan VV, Simkovsky R, Watrous JD, Trial RM, Fleming TC, et al. Primer on agar-based microbial imaging mass spectrometry. J Bacteriol. 2012;194(22):6023–8. https://doi.org/10.1128/jb.00823-12.
26. Buchberger AR, DeLaney K, Johnson J, Li L. Mass spectrometry imaging: a review of emerging advancements and future insights. Anal Chem. 2018;90(1):240–65. https://doi.org/10.1021/acs.analchem.7b04733.
27. Peukert M, Matros A, Lattanzio G, Kaspar S, Abadía J, Mock HP. Spatially resolved analysis of small molecules by matrix-assisted laser desorption/ionization mass spectrometric imaging (MALDI-MSI). New Phytol. 2012;193(3):806–15. https://doi.org/10.1111/j.1469-8137.2011.03970.x.
28. Guenther S, Koestler M, Schulz O, Spengler B. Laser spot size and laser power dependence of ion formation in high resolution MALDI imaging. Int J Mass Spectrom. 2010;294(1):7–15. https://doi.org/10.1016/j.ijms.2010.03.014.
29. Kompauer M, Heiles S, Spengler B. Autofocusing MALDI mass spectrometry imaging of tissue sections and 3D chemical topography of nonflat surfaces. Nat Methods. 2017;14(12):1156–8. https://doi.org/10.1038/nmeth.4433.
30. Gabriel SJ, Schwarzinger C, Schwarzinger B, Panne U, Weidner SM. Matrix segregation as the major cause for sample inhomogeneity in MALDI dried droplet spots. J Am Soc Mass Spectrom. 2014;25(8):1356–63. https://doi.org/10.1007/s13361-014-0913-0.
31. Pei X-L, Liu X-N, Du J-L, Gong C, Xu X. MALDI-MS imaging of lipids in corn using a flexible ultrasonic spraying device as matrix deposition method. Int J Mass Spectrom. 2020;455:116373. https://doi.org/10.1016/j.ijms.2020.116373.
32. Fournier I, Tabet JC, Bolbach G. Irradiation effects in MALDI and surface modifications: part I: sinapinic acid monocrystals. Int J Mass Spectrom. 2002;219(3):515–23. https://doi.org/10.1016/S1387-3806(02)00704-2.
33. Fournier I, Marinach C, Tabet JC, Bolbach G. Irradiation effects in MALDI, ablation, ion production, and surface modifications. Part II: 2,5-dihydroxybenzoic acid monocrystals. J Am Soc Mass Spectrom. 2003;14(8):893–9. https://doi.org/10.1016/S1044-0305(03)00347-7.
34. McDonnell LA, Mize TH, Luxembourg SL, Koster S, Eijkel GB, Verpoorte E, et al. Using matrix peaks to map topography: increased mass resolution and enhanced sensitivity in chemical imaging. Anal Chem. 2003;75(17):4373–81. https://doi.org/10.1021/ac034401j.
35. Moskovets E, Karger BL. Mass calibration of a matrix-assisted laser desorption/ionization time-of-flight mass spectrometer including the rise time of the delayed extraction pulse. Rapid Commun Mass Spectrom. 2003;17(3):229–37. https://doi.org/10.1002/rcm.898.
36. Xiang B, Prado M. An accurate and clean calibration method for MALDI-MS. J Biomol Tech. 2010;21(3):116–9.
37. Hart PJ, Francese S, Claude E, Woodroofe MN, Clench MR. MALDI-MS imaging of lipids in ex vivo human skin. Anal Bioanal Chem. 2011;401(1):115–25. https://doi.org/10.1007/s00216-011-5090-4.
38. Tiquet M, La Rocca R, Van Kruining D, Martinez-Martinez P, Eppe G, De Pauw E, et al. Mass spectrometry imaging using dynamically harmonized FT-ICR at million resolving power: rationalizing and optimizing sample preparation and instrumental parameters. ChemRxIv. 2020. https://doi.org/10.26434/chemrxiv.13013900.v1.
39. Cox J, Michalski A, Mann M. Software lock mass by two-dimensional minimization of peptide mass errors. J Am Soc Mass Spectrom. 2011;22(8):1373–80. https://doi.org/10.1007/s13361-011-0142-8.
40. Boskamp T, Lachmund D, Casadonte R, Hauberg-Lotte L, Kobarg JH, Kriegsmann J, et al. Using the chemical noise background in MALDI mass spectrometry imaging for mass alignment and calibration. Anal Chem. 2020;92(1):1301–8. https://doi.org/10.1021/acs.analchem.9b04473.
41. Palmer A, Phapale P, Chernyavsky I, Lavigne R, Fay D, Tarasov A, et al. FDR-controlled metabolite annotation for high-resolution imaging mass spectrometry. Nat Methods. 2017;14(1):57–60. https://doi.org/10.1038/nmeth.4072.